

RESEARCH

Open Access



A physiologically-based flow network model for hepatic drug elimination III: 2D/3D DLA lobule models

Vahid Rezania^{1*}, Dennis Coombe² and Jack A. Tuszynski³

* Correspondence:

rezaniav@macewan.ca

¹Department of Physical Sciences,
MacEwan University, Edmonton, AB
T5J 4S2, Canada

Full list of author information is
available at the end of the article

Abstract

Background: One of the major issues in current pharmaceutical development is potential hepatotoxicity and drug-induced liver damage. This is due to the unique metabolic processes performed in the liver to prevent accumulation of a wide range of chemicals in the blood. Recently, we developed a physiologically-based lattice model to address the transport and metabolism of drugs in the liver lobule (liver functional unit).

Method: In this paper, we extend our idealized model to consider structural and spatial variability in two and three dimensions. We introduce a hexagonal-based model with one input (portal vein) and six outputs (hepatic veins) to represent a typical liver lobule. To capture even more realistic structures, we implement a novel sequential diffusion-limited aggregation (DLA) method to construct a morphological sinusoid network in the lobule. A 3D model constructed with stacks of multiple 2D sinusoid realizations is explored to study the effects of 3D structural variations. The role of liver zonation on drug metabolism in the lobule is also addressed, based on flow-based predicted steady-state O₂ profiles used as a zonation indicator.

Results: With this model, we analyze predicted drug concentration levels observed exiting the lobule with their detailed distribution inside the lobule, and compare with our earlier idealized models. In 2D, due to randomness of the sinusoidal structure, individual hepatic veins respond differently (i.e. at different times) to injected drug. In 3D, however, the variation of response to the injected drug is observed to be less extreme. Also, the production curves show more diffusive behavior in 3D than in 2D.

Conclusion: Although, the individual producing ports respond differently, the average lobule production summed over all hepatic veins is more diffuse. Thus the net effect of all these variations makes the overall response smoother. We also show that, in 3D, the effect of zonation on drug production characteristics appears quite small. Our new biophysical structural analysis of a physiologically-based 3D lobule can therefore form the basis for a quantitative assessment of liver function and performance both in health and disease

Background

The liver is a complex organ that removes chemicals, including drugs, from the blood through metabolic processes. When such liver detoxification processes are incomplete or overwhelmed, liver damage can result leading to liver failure. Drug access to hepatocytes is governed by transport processes in the well-vascularized liver tissue, and so structural variability can impact such transport. Therefore, a quantitative understanding of drug distribution and metabolism in the liver is essential for the ability to predict both liver performance and damage. We envisage a future generation of algorithms for anatomically- and physiologically-based liver models that can be then used for the prediction of optimal doses and scheduling of various drugs prior to clinical administration. This could be especially useful for patients with liver diseases such as hepatocellular carcinoma or cirrhosis.

Several investigators have recently explored computational fluid models of liver lobule function. Ierapetritou et al. [1] give a comprehensive general overview of the modeling approaches and issues that arose up to 2009. More particularly, Rani et al. [2] developed a detailed computational dynamics model of a small portion of a liver lobule, focusing on the non-Newtonian characteristics of blood. They considered the flow along one sinusoid with exit fenestrations fed by a portal vein and hepatic artery segments and exiting via a hepatic vein segment. The contributions of portal vein (PV) versus hepatic artery (HA) flows to the overall pressure drop and velocity profiles were detailed, including regions of Eddie flows and high strain rates near the exit fenestrations. Steady state flows were achieved after 5×10^{-5} s.

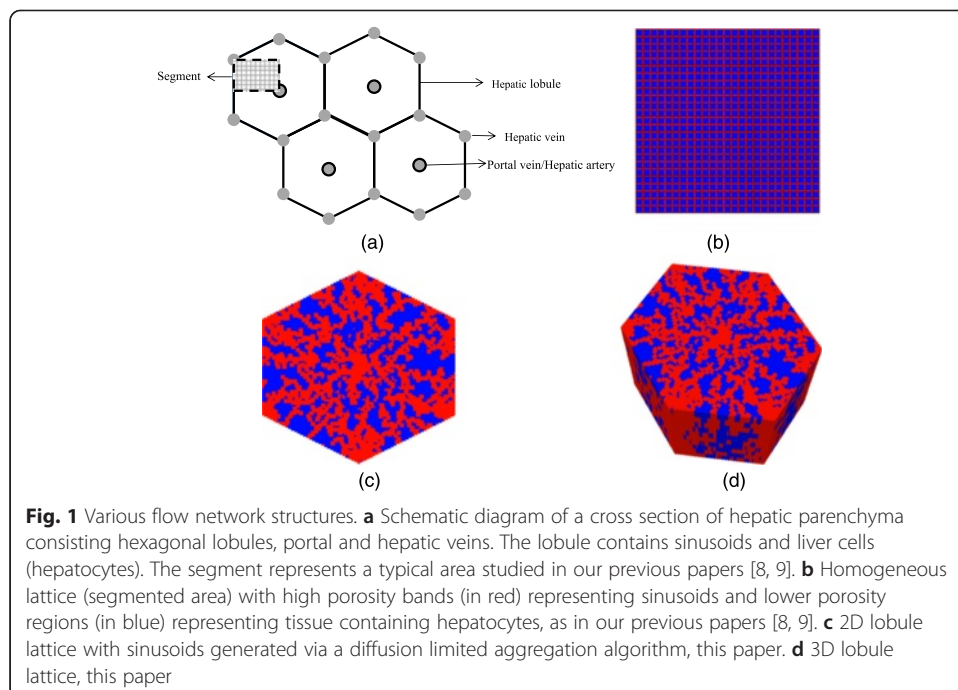
Yan et al. [3] developed a physiologically-based, multi-agent model of liver lobule performance. They used a Monte Carlo selection method to determine properties of the sinusoidal graph structure, convective-dispersive flow and metabolic interactions. This allowed inclusion of lobule zonation effects plus the metabolic influences of chemical molecular weight, octanol partition coefficients and protein binding to predicted drug-liver lobule interactions. They matched lobule outflow characteristics of 4 cationic drugs (atenolol, antipyrine, labetalol, and diltiazem), using sucrose as a base flow chemical. Wambaugh and Shah [4] compared the role of various lobule (sinusoidal) morphologies on drug propagation again using an agent-based simulation approach. While demonstrating that their model can reproduce traditional coarse averaging results (well-mixed and parallel tubes) under some flow regimes, they emphasized the utility of their random statistical approach for rapidly metabolized chemicals.

Hoehme et al. [5] employed a combined experimental and computational study of lobule structural restoration after CCl_4 damage over several days as a protocol for liver regeneration. They used agent-based representations of both hepatocytes and sinusoids in their computational model and demonstrated that the regeneration process is characterized by a hepatocyte-sinusoid alignment process to correctly restore liver micro-architecture. Schliess et al. [6] extended this approach to consider ammonia detoxification during liver damage and regeneration. Here they first proposed a simple metabolic model considering ammonia, urea, and glutamine components utilizing three mass balance ordinary differential equations (ODEs) for chemical reactions and two compartments (periportal and perivenal) such that urea generation is maximized in the periportal region while glutamine regeneration occurs perivenally. The resulting

concentrations were interpolated on their spatial-temporal grid as the sizes of the damaged zones change over the regeneration process. They also considered a multi-lobule pattern to reduce boundary effects. Drasdo et al. [7] summarized both modeling approaches in a review article.

In previous papers (papers I [8] and II [9]), we proposed a physiologically-based lattice model to study the transport and metabolism of drugs in the liver lobule. In these studies, we constructed a simple regular square lattice model that represents a portion of a liver lobule, see Fig. 1a and b, to explore the dynamics of competing convective, diffusive, and reactive processes acting on an injected chemotherapeutic drug paclitaxel. Structural and spatial variations and liver lobule zonation were also considered and their impacts on the hepatic drug metabolism were discussed. Such simulations had the useful consequence of interpreting drug concentration levels found exiting the lobule in terms of their detailed spatial distribution within the lobule, caused by competing processes. This analysis forms the basis, and a point of contrast, to the drug distributions obtained when some of these basic assumptions on lobule structure are relaxed.

In this paper, we extend our biophysical structural analysis to a full lobule situation, a hexagonal based model with one central blood in-flow (portal vein) and six corner located out-flows (hepatic veins), see Fig. 1. We also introduce the sinusoid network using a sequential diffusion-limited aggregation (DLA) algorithm (as presented and discussed below, Fig. 3) to gain insight on a more realistic resulting morphological sinusoid structure, see Fig. 1c. In a nutshell, sequential means a series of DLA generated pattern steps (5 steps) to generate the desired sinusoid structure variations in 2D. Thereafter we repeat this algorithm for various layers to generate a representative 3D lobule pattern. As a result, individual sinusoid layers, although generated by the same DLA algorithm, are not identical



but exhibit some variability as observed in real lobules. A sensitivity analysis is conducted by observing drug concentration levels exiting the lobule with their predicted detail distribution inside the lobule.

The liver lobule functional unit

It is commonly accepted that a single lobule serves as the functional unit of the liver, the smallest structural unit of the liver with ability to perform all hepatic functionalities [10]. The classic lobule is a hexagonal cylinder, centered around a hepatic venule and with portal tracts situated at the corners. The portal lobule has a similar shape but is centered about a portal tract with the hepatic venules at the periphery [11]. We shall invoke this second point of view as the basis for our model development.

Even among the approximately 1.5 million lobules (assuming a liver size of 1500 cm^3 and a lobule size of 1 mm^3) that make up the human liver, structural variability of lobule units is the rule. Teutsch and colleagues [12] illustrate this specific microarchitecture variability and diseased states can be expected to add additional variability. Here we will attempt to quantify the consequences of such variability via our computational model.

Methods

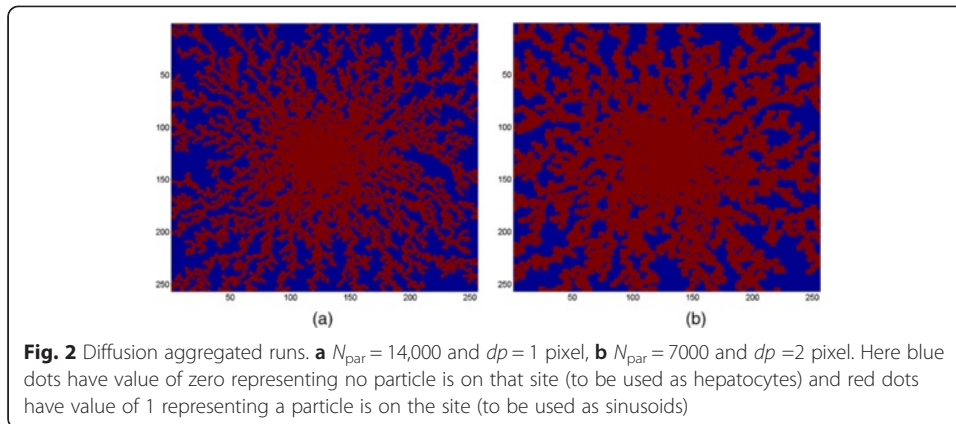
2D hexagonal lobule construction

The flow equations describing reactive-convective-diffusive flow in the liver lobule remain unchanged from our first two papers. Figure 1a and b illustrate the network structure of our base case model discussed in papers I [8] and II [9] (which uses a regular sinusoid pattern). Figure 1c represents our model that we study here, which consists of a 2D square lattice clipped by hexagonal boundary with DLA constructed sinusoid network. Figure 1d demonstrates a 3D extension of the lobule model that will be discussed later.

In this paper, MATLAB [13] has been used to code and generate sinusoid network using a novel sequential DLA algorithm. We use a standard DLA algorithm that randomly clusters a specified number of particles (here N_{par}) with particle size ($dp \times dp$ in a pixel²). Figure 2a and b show result of DLA runs for $N_{\text{par}} = 14,000$ and $dp = 1$ pixel and for $N_{\text{par}} = 7000$ and $dp = 2$ pixel, respectively.

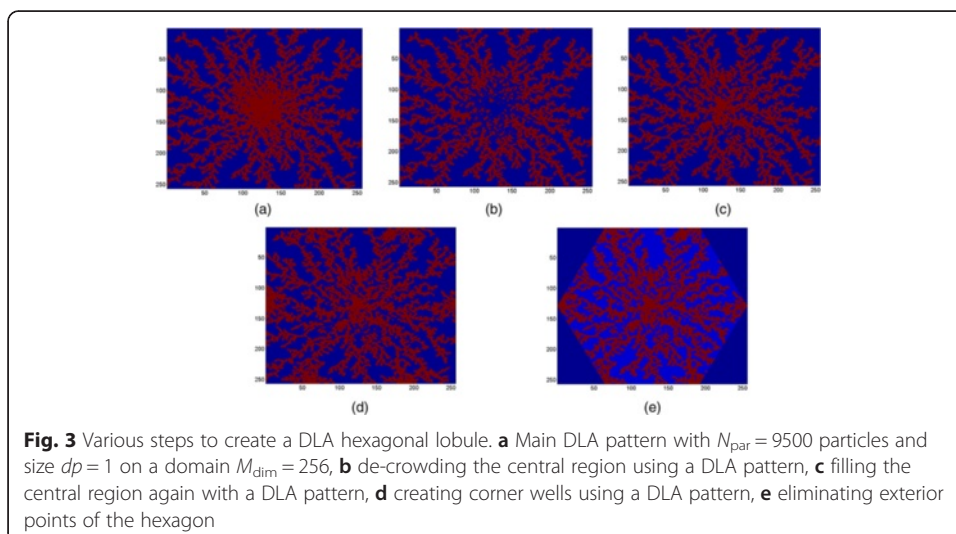
In order to create a hexagonal lobule comparable to a realistic liver lobule, five steps are taken:

- i) A zero $M_{\text{dim}} \times M_{\text{dim}}$ matrix (field) has been created and the DLA algorithm has been called to create a DLA pattern with specified N_{par} and dp . A particle, valued 1, has been located at a random position in the field by the DLA algorithm and then performed a random walk (with a desired step size, here denoted by dp) toward the center of the field. The newer particle will do the same until it hits another (older) particle, sticks to it and stops. This will continue for all $N_{\text{par}} = 9500$ particles. See Fig. 3a. Here $M_{\text{dim}} = 256$ and $dp = 1$.
- ii) As shown in Fig. 3a, the central region is very crowded. We overwrite the central region (here we chose half-the original field) using the DLA algorithm and with



- smaller number of zero-valued particles (blue dots). Here we use $N_{\text{cen1_par}} = 1200$, $M_{\text{dim}} = 128$ and $dp = 1$. See Fig. 3b.
- iii) To fill the central region with sinusoids again (red dots), the DLA algorithm will be called for the third time with fewer particles, i.e. $N_{\text{cen2_par}} = 800$. Here $M_{\text{dim}} = 128$ and $dp = 2$. See Fig. 3c.
 - iv) In this step, we determine the six corners of the hexagon to create the out-flowing wells at these locations. Again the DLA algorithm will be used to create a DLA pattern around each corner. See Fig. 3d. Here we use the domain size of $1/3$ of the original domain, i.e. $M_{\text{dim}}/3$, and fewer particles, $N_{\text{cor_par}} = 500$. Here $dp = 1$.
 - v) At the final stage, any point outside the bounding hexagon is removed. Figure 3e shows the final result if the DLA hexagonal lobule. As shown, hepatocytes are blue islands that are encompassed by red sinusoids.

This sinusoid generation algorithm is similar in spirit but not in details to that employed by Wambaugh and Shah [14]. They have used the term “sinusoid morphology” to characterize these investigations, which we will also employ. In recent work, Hoehme et al. [15] captured realistic lobule sinusoid patterns from image analysis of confocal microscopy of liver tissue. To check whether our simulated sinusoid pattern is



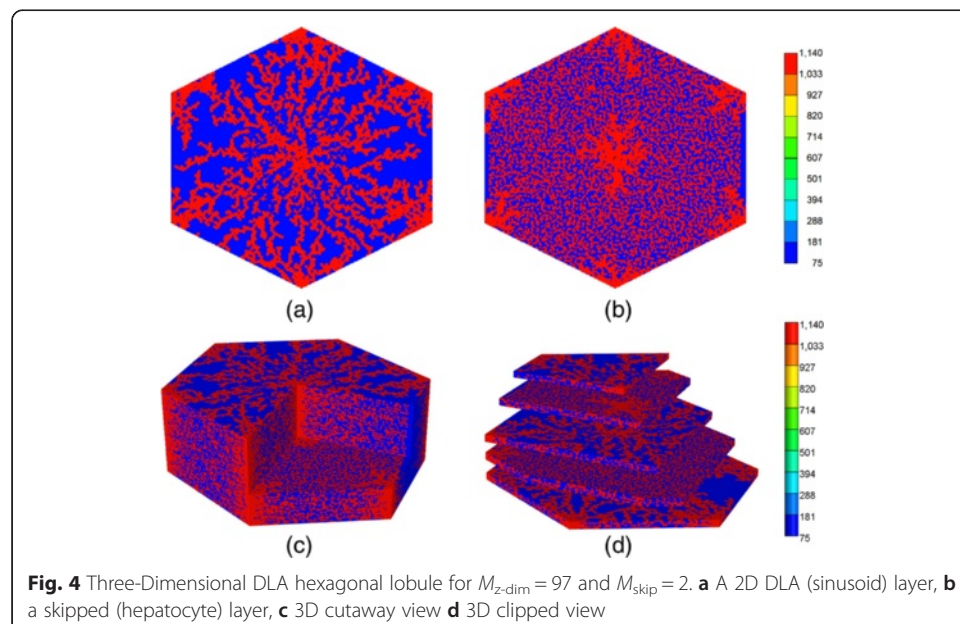
comparable with their result, we perform a population density analysis for several 2D simulated and real lobules (Wisk S, Rezania V: A comparison between real and DLA simulated liver lobules using a population density analysis, Submitted). We calculated the ratio of the area covered by sinusoids to the total area of the lobule for both simulated and real 2D lobule images to optimize values of N_{par} and dp for corresponding M_{dim} . Based on these calculations, we find $N_{\text{par}} \approx 37 M_{\text{dim}}$ (~ 9500) and $dp = 1$ will produce comparable results ($\sim 45\%$ sinusoid area/total 2D area). A comparison of our Fig. 3d with their results demonstrates that our DLA algorithm with the chosen parameters generates equally physiologically reasonable sinusoid morphology patterns (in particular, see their Fig. 1d or further details in their SI Appendix, their Fig. 3d).

Extension to a 3D lobule structure

In order to generate an even more realistic survey, we next study a 3-dimensional lobule. Again our morphological sinusoid generation algorithm is similar in spirit to that employed by Wambaugh and Shah [14] in their 3D models.

The 3D DLA structure is essentially constructed by stacking several 2D DLA structures as follows:

- i) A vertical dimension $M_{z\text{-dim}}$ will be specified.
- ii) Starting from the very bottom layer that has a 2D DLA structure, we skip M_{skip} layers to introduce the next layer with a 2D DLA structure (a DLA layer), see Fig. 4a. This procedure will be repeated to reach to the very top layer which again is a DLA layer. Here, each DLA layer represents the sinusoidal network. Two of these layers encompass hepatocyte cells (the skipped layers). The value of M_{skip} is chosen based on the average thickness size of a hepatocyte cell.
- iii) Then, two DLA layers vertically will be connected at several random locations to approximate the shape hepatocyte cells, see Fig. 4b.



- iv) The center and the six corners of the hexagon in all layers will be connected to represent arterial and portal veins.

Since the skipped layers represent the hepatocyte tissue, the value of M_{skip} will be determined based on the typical volume of a lobule and hepatocytes. The typical volume of a human liver lobule is somewhat less than 1 mm^3 [12]. Furthermore, a hepatocyte has a diameter of $12 - 24 \text{ }\mu\text{m}$ and thickness of $25 \text{ }\mu\text{m}$ in average and mean sinusoid thickness is about $5 - 7 \text{ }\mu\text{m}$. Here, we chose a sinusoidal cell as a cube with dimension of $6 \text{ }\mu\text{m}$ and a hepatocyte cell as rectangular cube with dimensions $6 \text{ }\mu\text{m}$ and $12 \text{ }\mu\text{m}$, with thickness of $6 \text{ }\mu\text{m}$ in the DLA layers and $12 \text{ }\mu\text{m}$ in the skipped layers, respectively. The area of a hexagon with diameter of d is given by $S = 3\sqrt{3}d^2/8$.

In our case, $d = 256 \times 6 \text{ }\mu\text{m} = 1536 \text{ }\mu\text{m}$ that leads to $S = 1.53 \times 10^6 \text{ }\mu\text{m}^2$. The 3D lobule is then composed by stacking up 33 sinusoidal layers and 64 tissue layers ($M_{z\text{-dim}} = 97$) that gives an approximate model volume of 1.5 mm^3 . Here, every two tissue layers are sandwiched by two sinusoidal layers ($M_{\text{skip}} = 2$). This choice of tissue/sinusoid grid thickness represents a compromise between simulation runtime speed and numerical discretization error.

Figure 4 shows the 3D DLA hexagonal lobule for $M_{z\text{-dim}} = 97$ and $M_{\text{skip}} = 2$. Figure 4a demonstrates a 2D DLA layer representing a sinusoidal layer. Figure 4b shows a hepatocyte layer. The red points connect all hepatocyte layers between two DLA layers. These points approximately determine the boundary of the hepatocyte cells. To construct the third dimension, a DLA layer is created for the bottom, then two hepatocyte layers ($M_{\text{skip}} = 2$), and then a new DLA layer will be produced. The procedure repeats over the whole z -dimension. Figures 4c and d show two different 3D views.

Flow calculation methods

Convection-diffusion-reaction flow calculations are performed on the generated models utilizing the STARS advanced process simulator [16] as described in our earlier papers. Here we have chosen paclitaxel (PAC) [17] as our example drug, as it is one of the most widely used chemotherapy agents, especially active against many human solid tumors [18] (breast cancer, ovarian cancer, lung cancer, etc). Table 1 summarizes our base

Table 1 Base case flow and metabolism parameters

Parameter	Characteristic (SI) Unit	STARS Unit
Sinusoid Porosity ϕ_{sin}	0.7854	0.7854
Sinusoid Permeability K_{sin}	$1.125 \text{ }\mu\text{m}^2$	1.140 Darcy^a
Sinusoid Effective Diffusion D_{sin}	$4.2 \times 10^{-10} \text{ m}^2/\text{s}$	$2.5 \times 10^{-4} \text{ cm}^2/\text{min}$
Tissue Porosity ϕ_{tis}	0.2382	0.2382
Tissue Permeability K_{tis}	$7.35 \times 10^{-2} \text{ }\mu\text{m}^2$	$7.45 \times 10^{-2} \text{ Darcy}$
Tissue Effective Diffusion D_{tis}	$4.2 \times 10^{-11} \text{ m}^2/\text{s}$	$2.5 \times 10^{-5} \text{ cm}^2/\text{min}$
Maximum Rate v_{max}^b	$0.06 \text{ }\mu\text{M}/\text{min}$	$1.08 \times 10^{-9} \text{ mole fraction}/\text{min}$
Half Saturation Constant K_m^b	$10.0 \text{ }\mu\text{M}$	$1.8 \times 10^{-7} \text{ mole fraction}$
Linear Rate v_{max}/K_m^b	$6.0 \times 10^{-3} \text{ min}^{-1}$	$6.0 \times 10^{-3} \text{ min}^{-1}$
Blood Viscosity μ	$3.5 \times 10^{-3} \text{ Pa}\cdot\text{sec}$	3.5 cpoise

^a $1 \text{ Darcy} = 0.9869 \text{ }\mu\text{m}^2$ in engineering permeability units

^b PAC kinetic elimination Michaelis-Menten parameters converted from Vaclavikova et al. [17], their Table 4

case flow and metabolic parameters for PAC (from Vaclavikova et al. [19]) used in these calculations for a representative human lobule. Cytochrome P450 CYP2C8 or CYP3A4 [20] are the enzymes active in PAC metabolism. Due to the non-regular areal sinusoidal structures generated here, however, it was found necessary to utilize a higher order discretization method (“areal 9-point”) to produce the expected smooth profiles on these grids. A discussion of this (quite standard) discretization method can be found in the STARS manual.

Results and Discussion

2D drug distribution – comparison to our earlier studies

Similar to previous studies, flow is induced in the lobule lattice by applying a pressure difference across the central inlet and six corner outlet points. With the chosen lobule flow parameters for porosity, permeability, and blood viscosity, the steady flow rate is $4.491 \times 10^{-6} \text{ cm}^3/\text{min}$ with $(0.4077, 0.3011, 0.1950, 0.9682, 0.2251, 2.394) \times 10^{-6} \text{ cm}^3/\text{min}$ for ports A to F, respectively, as illustrated in Fig. 5. (For steady flows, the inflow rate equals the total outflow rate.) It is clear that ports D and F have highest outflow among the others. This is due to the random nature of the DLA simulation for this realization.

Figure 6 demonstrates the steady state velocity profile throughout the lobule lattice, illustrating both the diverging/converging nature of the flow near the inlet and outlet ports (i.e. injector and producers, respectively), as well as the orders of magnitude difference of the flows in the sinusoids and tissues, respectively. (This plot uses a logarithmic colour scale axis). Ports D and F show highest velocities among the ports.

Blood with a relative composition of 1 microgram PAC (1.8×10^{-8} mole fraction) is infused into the lobule through the central inlet. Assuming nonreactive hepatocytes, the time required to traverse the lattice is approximately 1 min or less as demonstrated in Fig. 7. The fastest drug propagation is through ports D and F for this realization. Similar to our Paper I [8], this production profile is convective flow dominated as the addition of diffusion minimally alters the production profile (figure not shown).

As indicated in our Paper II [9] concerning variable lattices models with multiple realizations, flow induced by the application of a fixed pressure drop across a lobule model can be expected to vary significantly for each model realization. This will in turn

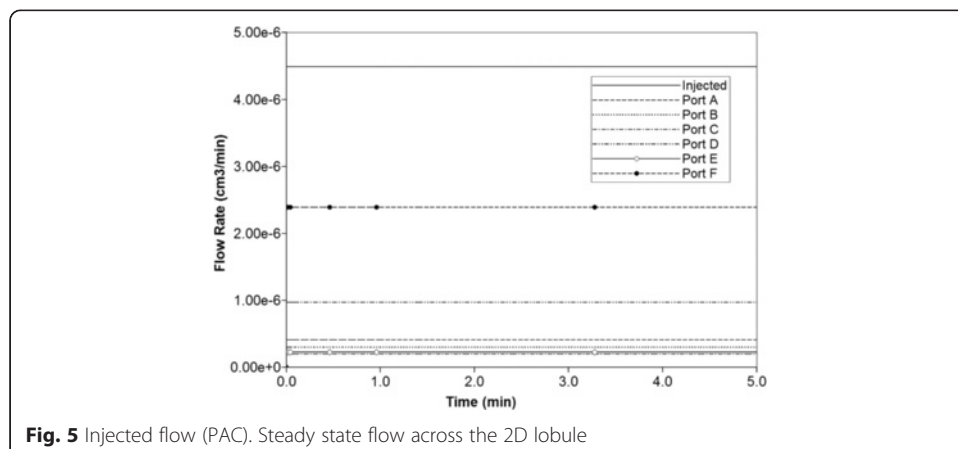
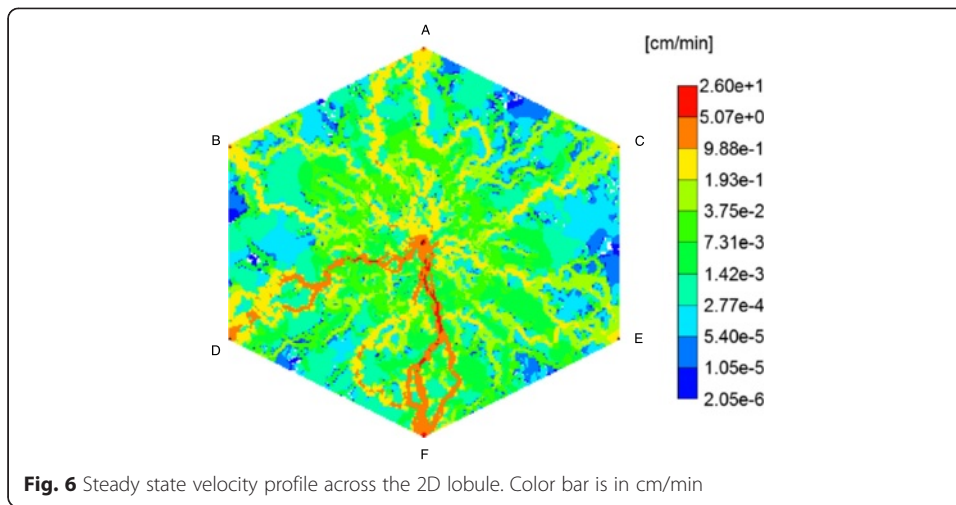


Fig. 5 Injected flow (PAC). Steady state flow across the 2D lobule



impact on the propagation and production characteristics of both non-reactive and metabolized drugs. Thus multiple realizations of the morphological sinusoidal network generated by our DLA algorithm here induce a similar variability in flow and drug production behavior. Table 2 summarizes the flow variability for 16 such realizations. In what follows, we will focus on the analysis of drug behavior for one such realization.

The spatial progression of the PAC concentration on the lobule lattice without and with diffusion is demonstrated in Figs. 8 and 9, respectively. The diffusion constants for PAC and PAC-OH are estimated as $2.5 \times 10^{-4} \text{ cm}^2/\text{min}$ in sinusoid and $2.5 \times 10^{-5} \text{ cm}^2/\text{min}$ in tissue, respectively. In the absence of diffusion, only a small “pressure-difference-driven (convective)” transfer from sinusoids to tissue through the space of Disse is occurring. See our Paper I [8] for details.

Figures 8 and 9 show the increasing levels of injected drug from 0.01 min to 5 min (0.5 min in case with diffusion). As shown, by 0.01 min, PAC almost reaches the outgoing port F of the lobule.

In case with no diffusion, it takes almost 5 min to fill the lobule (Fig. 8), while PAC completely covers the lattice after 0.5 min when diffusion is on as demonstrated in Additional file 1: Figure S1.

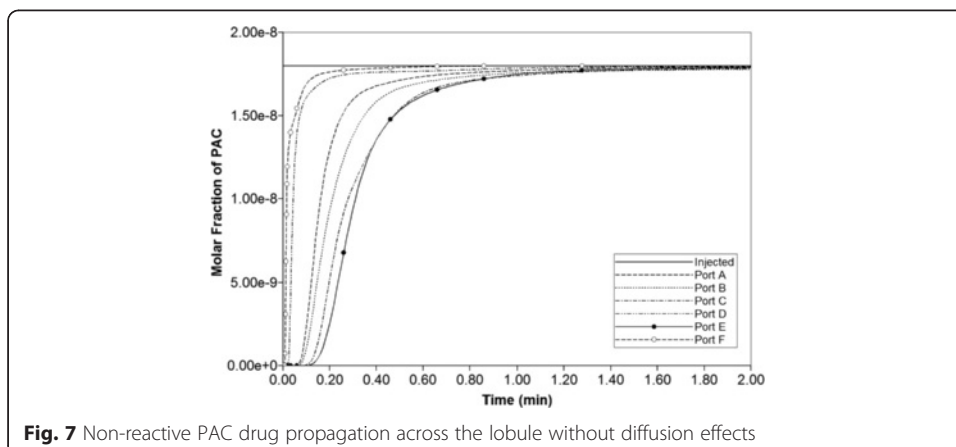


Table 2 Flow rate variability of multiple 2D DLA sinusoid morphologies

Layer no.	SS flow rate ($\times 10^{-5}$ cm ³ /min)
Lyr1	1.824
Lyr4	1.366
Lyr7	1.829
Lyr10	0.776
Lyr13	1.781
Lyr16	1.716
Lyr19	1.399
Lyr22	0.889
Lyr25	1.555
Lyr28	1.225
Lyr31	1.684
Lyr34	1.416
Lyr37	1.251
Lyr40	1.044
Lyr43	1.421
Lyr46	1.983
Average	1.447
STDEV	0.3511

Reactive flows in 2D

Now we consider the effects of PAC drug metabolism by hepatocytes. Here the base case reaction parameters of Table 3 of Paper I [8] are employed, and the same injected PAC concentration (1.8×10^{-8} mole fraction) is considered. With the employed reaction half saturation constant value of 1.8×10^{-7} mole fraction, this injection level implies the Michaelis-Menten model reduces to an almost linear reaction equation.

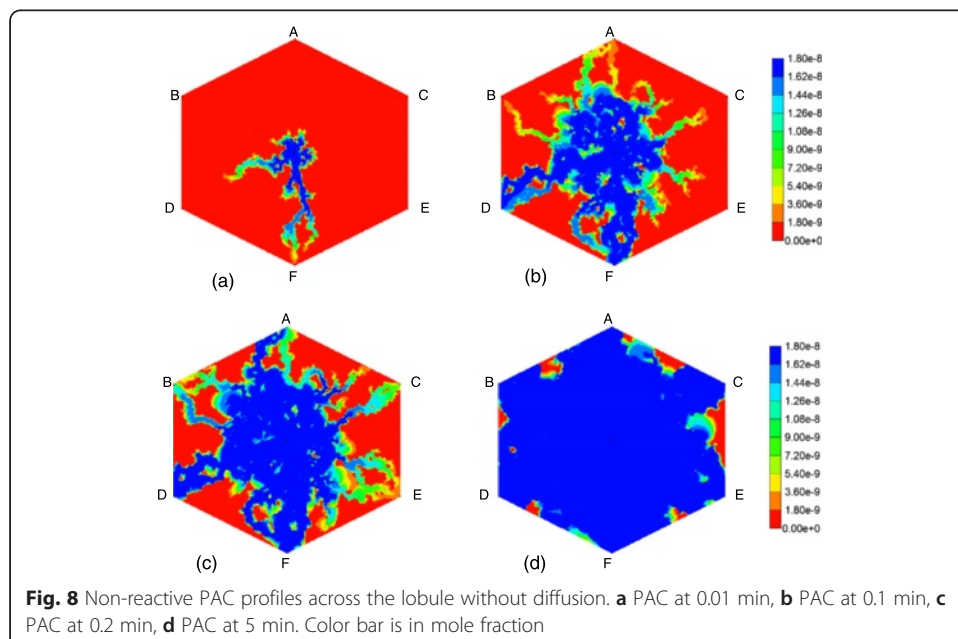


Fig. 8 Non-reactive PAC profiles across the lobule without diffusion. **a** PAC at 0.01 min, **b** PAC at 0.1 min, **c** PAC at 0.2 min, **d** PAC at 5 min. Color bar is in mole fraction

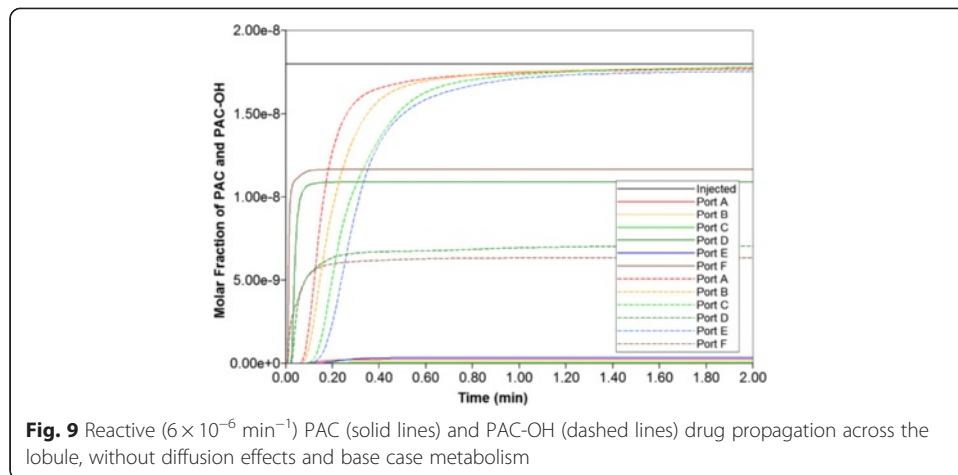
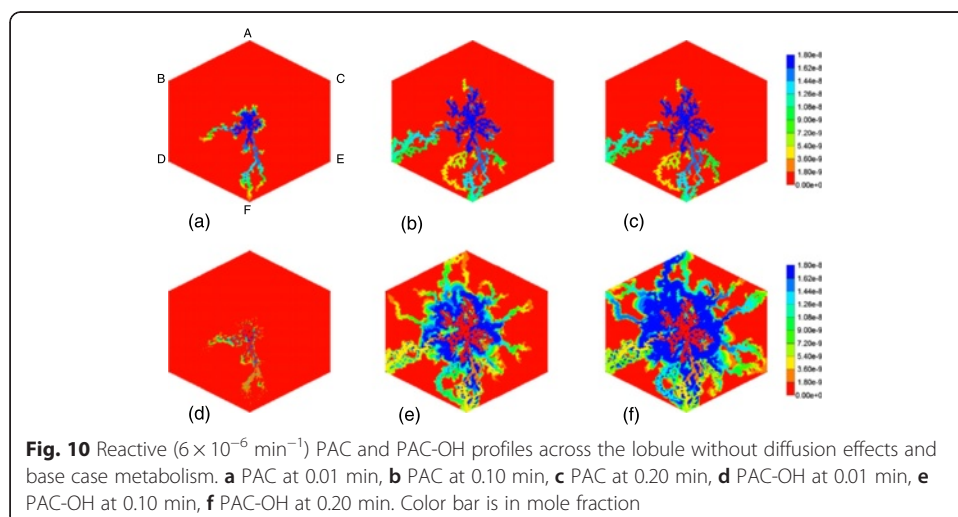
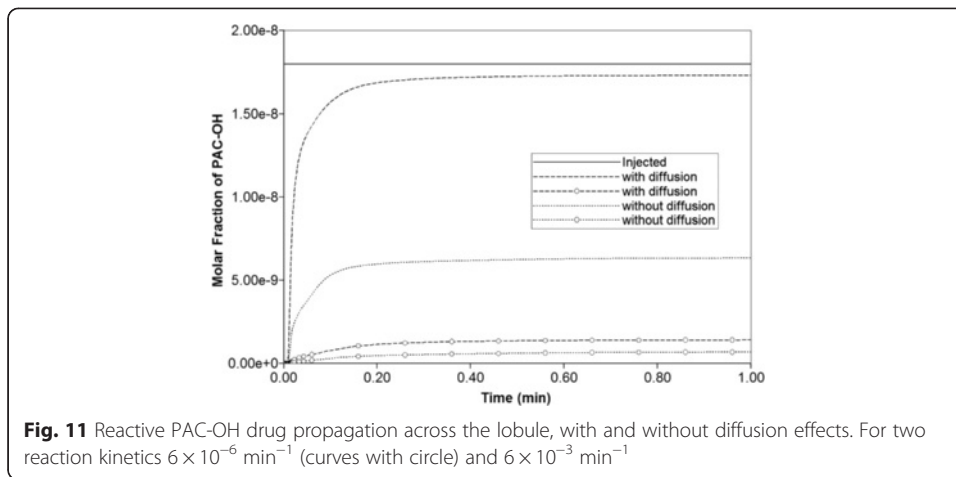


Figure 9 illustrates injected drug and produced drug and metabolite production for this case. The reaction rate is $6 \times 10^{-3} \text{ min}^{-1}$. Again it is emphasized that both PAC and PAC-OH have assumed equal diffusive flow contributions, as these are components of very similar size. Essentially at this reaction rate, all injected PAC is converted to metabolite by the lobule hepatocytes. The production profile of PAC-OH here is similar to the production profile of PAC in the non-reaction case, as shown in Fig. 7, for most of the ports. That is, the reactive conversion of PAC to PAC-OH occurs reasonably quickly. However, for the two ports with higher flows (ports D and F), less conversion of PAC to PAC-OH is seen to occur.

Figure 10 shows the PAC and PAC-OH profiles across the lobule lattice at 0.01 min, 0.10 min, and 0.20 min, respectively. The PAC concentrations in the sinusoids and the PAC-OH concentrations in the tissue are equivalent to the PAC concentrations in both sinusoids and tissue for the non-reacted case (Fig. 8). Note that after 0.1 min there is no change in PAC spatial distribution as it converts to PAC-OH before propagating further. Figure 10 also shows clearly there is an inlet distance over which the reaction conversion time is not fast enough to convert the injected PAC.



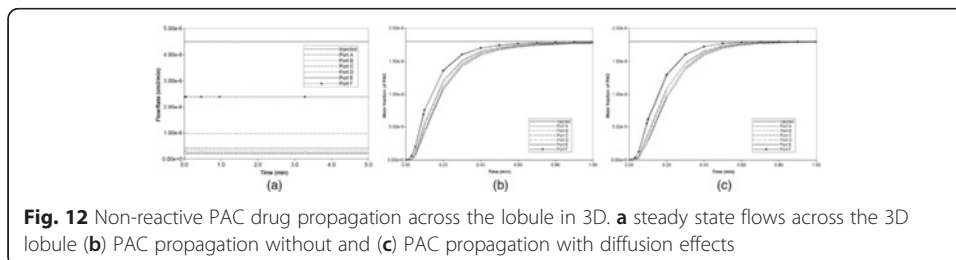


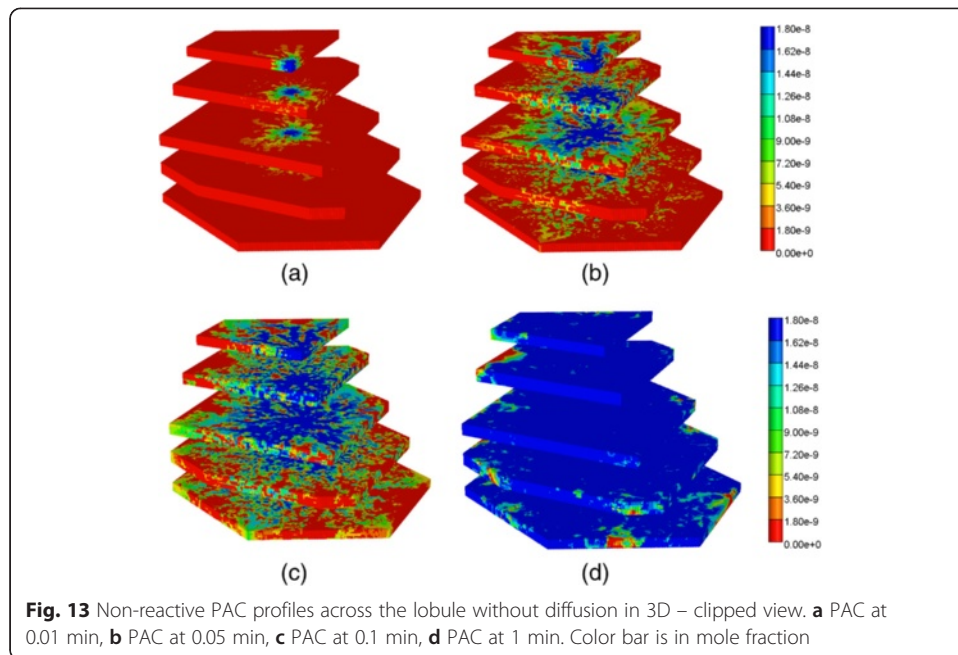
Diffusion, however, has greater impacts on the reactive cases. Figure 11 compares the overall PAC to PAC-OH conversion for two reactive cases with reaction rate $6 \times 10^{-6} \text{ min}^{-1}$ and $6 \times 10^{-3} \text{ min}^{-1}$, with and without diffusion. (The latter rate is our base case which has the higher conversion rate.) As shown, at each rate a greater concentration of PAC-OH is generated when diffusion is on, as this provides an additional mechanism to bring PAC molecules to the reactive hepatocyte sites.

3D drug distribution – extension of behaviors

As stated above, the 3-dimensional lobule is constructed by stacking up 33 sinusoidal layers and 64 hepatocyte layers ($M_{z\text{-dim}} = 97$) with the approximate volume of 1.5 mm^3 . The sinusoidal layers have similar structures (randomly generated though) as the 2D DLA lobule structure discussed in previous section. The hepatocyte layers are generated by randomly selected points to mimic hepatocyte cell distribution in a lobule. All layers are connected through the central region (the portal vein) as well as six corners of the hexagon (hepatic veins). In this section we are interested in studying the effect of the third dimension as the blood will be injected from the central vein in all layers simultaneously.

In 3D, the steady flow rate across the full lobule is $3.00 \times 10^{-3} \text{ cm}^3/\text{min}$ as shown in Fig. 12a, as all volumes have been upscaled from our 2D slice models. As seen in Fig. 12b and c, in this realization of the 3D lobule, ports A and F have highest outflow (they are essentially superimposed), then ports B and D (they are essentially superimposed), with C and E having the lowest outflow rates. This is again due to the random nature of the DLA simulation for this realization. However the port-to-port variation in





flows is significantly less extreme in 3D, as the third dimension provides additional connecting flow paths to smooth the overall flow pattern.

Figure 13 gives a spatial view (clipped-view) of the increasing levels of the injected PAC drug from 0.01 min to 1 min across the lobule without diffusion and no reaction. The drug first clearly follows the high flow paths provided by the morphological sinusoid network, and only slowly reaches into the tissue portions of the lobule. A different spatial view (block-view) is also demonstrated in Additional file 2: Figure S5.

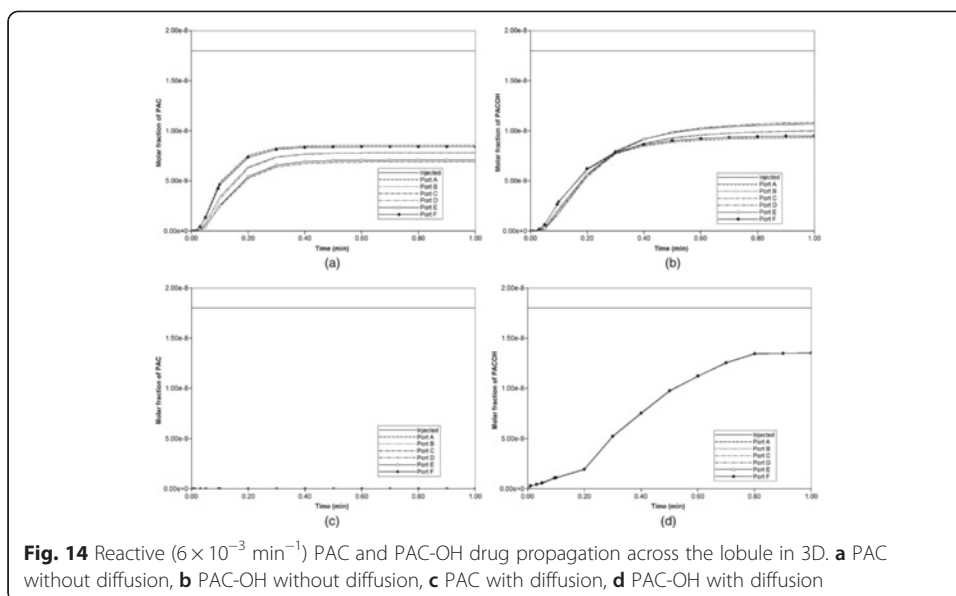
The same two views of non-reactive PAC injection with diffusion added are shown in Additional file 3: Figure S2 and Additional file 4: Figure S3. In those figures the sinusoid-tissue transfer rate is much more rapid and PAC drug propagates in a more uniform fashion as it enters the lobule. Clearly, diffusion has a very significant effect on the drug propagation details although at later times both cases result in a uniform drug coverage of the lobule.

Reactive flows in 3D

Now we consider the effects of PAC drug metabolism by hepatocytes across the 3D lobule. Similar to the 2D case, the same injected PAC concentration (1.8×10^{-8} mole fraction) is considered.

Figure 14 illustrates injected drug and produced drug and metabolite production for this case without and with diffusion effects. The reaction rate is $6 \times 10^{-3} \text{ min}^{-1}$. As before, both PAC and PAC-OH have assumed equal diffusive flow contributions.

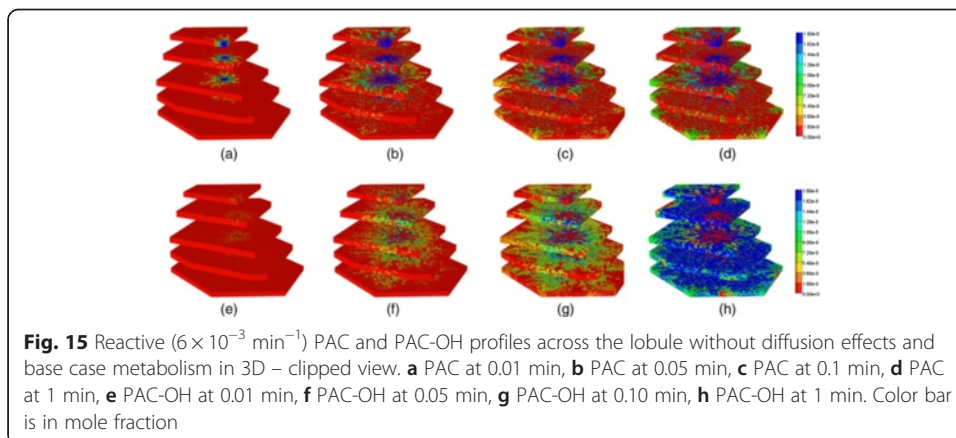
Figures 14a and b demonstrate the levels of PAC and PAC-OH, respectively, without including diffusion effects. As shown, both PAC and PAC-OH have similar concentrations after 1 min in all outlets (i.e. approximately half of injected PAC is metabolized to PAC-OH). The diffusion, however, alters the latter behavior significantly as depicted in Fig. 14c and d. All the PAC converted to PAC-OH almost immediately. The variability



of the produced PAC-OH concentration per port for this reactive case with diffusion mirrors the variability of the produced PAC per port for the nonreactive case (Fig. 11, with or without diffusion).

Figure 15 shows the spatial clipped-view of reactive PAC and PAC-OH distributions in the 3D lobule at selected times without diffusion effects and with the base case metabolism rate. As time progresses, more PAC is metabolized to PAC-OH but the metabolic rate is low enough that both PAC and PAC-OH distribute throughout the lobule. This distribution is not uniform throughout the lobule however. For example, there remains an inlet zone with a negligible amount of PAC-OH at all times. The spatial block-view is also demonstrated in Additional file 5: Figure S6.

As shown in Additional file 6: Figure S4, with diffusion but still utilizing a base case metabolic rate, the in-situ conversion of PAC to PAC-OH is much more rapid and uniform, and results in an almost total drug conversion to PAC-OH throughout the 3D lobule. There remains only a small inlet region of unconverted PAC.



As in the 2D cases presented earlier, diffusion has greater impact on drug distribution for the reactive cases. Similar behaviors can be observed for other reaction rates (e.g. reaction rate $6 \times 10^{-1} \text{ min}^{-1}$) with and without diffusion (not shown).

3D drug distribution with zonation

Zonation is a well-known feature of many metabolic processes in the liver lobule [15], some processes are up-regulated in the periportal region, while others are up-regulated in the perivenal region. Here we consider zonation of drug metabolizing enzymes (in particular cytochrome P450 – CYP2C8), such that higher CYP levels are found near the perivenal region.

Zonation has been attributed primarily to a non-uniform distribution of O_2 across the lobule [16]. Here we will utilize this experimental observation to predict relative CYP levels based on a calculated O_2 distribution. Appendix A presents details of the O_2 convective-diffusive-reactive flow problem employed to generate the zoned-CYP distribution.

The resultant initial non-homogeneous distribution of CYP enzymes is imported into the PAC reaction model in a manner analogous to that employed in our earlier idealized model of zonation [9]. Here we consider enhanced perivenal enzyme expression (the “reversed” case of reference [9]) as a reference, where CYP expression is active primarily near the lobule outlet zone. In our present work, two scenarios are envisioned: (a) a CYP distribution generated from “normal” levels of O_2 injection, and (b) that generated from a “low concentration” O_2 injection level. The result is shown in Figures A3 and A4, which can be contrasted to Additional file 3: Figure S2b of our earlier idealized model [9]. These distributions are used to modify the PAC metabolic rates non-homogeneously in a manner similar to our earlier paper.

Figure 16 compares reactive PAC and PAC-OH production profiles with no diffusion contributions to the flow. Note that both PAC and PAC-OH are produced here as in our ideal treatment of zonation found in Paper II [9]. In Fig. 16 only ports A and C are shown as their productions show the largest variation among all six production ports. Zonation (either averaged or extreme) is seen to have a small effect on the production behavior compared to the base case (no zonation) behavior, with the low concentration zonation profiles essentially identical to the no zonation case (see the almost uniform CYP profile generated for this case, Figure A3). Finally, with the same (reversed) zonation patterns, but assuming additional diffusive contributions to the flow, mostly only PACOH is produced, and no differences in production behavior are seen with or

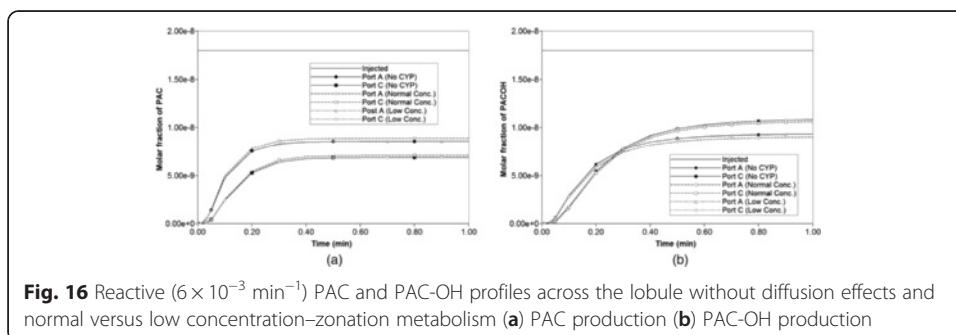


Fig. 16 Reactive ($6 \times 10^{-3} \text{ min}^{-1}$) PAC and PAC-OH profiles across the lobule without diffusion effects and normal versus low concentration–zonation metabolism (a) PAC production (b) PAC-OH production

without zonation (not shown). This is consistent with our ideal treatment of zonation described in Paper II [9].

Spatial plots of PAC and PACOH distributions at various time points for the no diffusion cases with zonation show only subtle differences from the base case no-zonation profiles of Fig. 16 and thus are not shown explicitly. This is perhaps not surprising for the low O₂ concentration generation case with a very uniform zoned CYP distribution, but is more puzzling for the normal O₂ concentration generated case. We believe this is a result of the high PAC to PACOH conversion rate chosen as our example for this paper coupled to the downstream distribution of CYP. This example appears to be quite robust to details of the exact CYP zonation pattern.

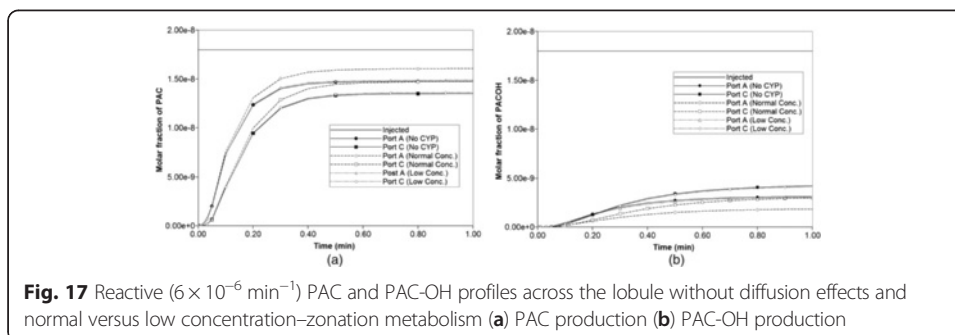
To further confirm these comments, we have rerun the models with a lower PAC metabolism rate. Figure 17 compares reactive PAC and PAC-OH production profiles with no diffusion contributions to the flow at these lower reaction rates ($6 \times 10^{-6} \text{ min}^{-1}$). Again only ports A and C are shown. For these cases, the low concentration zonation production is again essentially identical to the no zonation case, but the normal zonation production differs more substantially from the other two cases. This behaviour is reflected in the spatial distributions of PAC and PACOH at various time points as well. Figure 18 compares the final (at 1 min) spatial distributions for PAC and PACOH for the normal and low-oxygen concentration generated CYP distributions. (The no zonation case is essentially identical to the latter case plots, not shown). The normal oxygen generated CYP distribution results in less PACOH conversion.

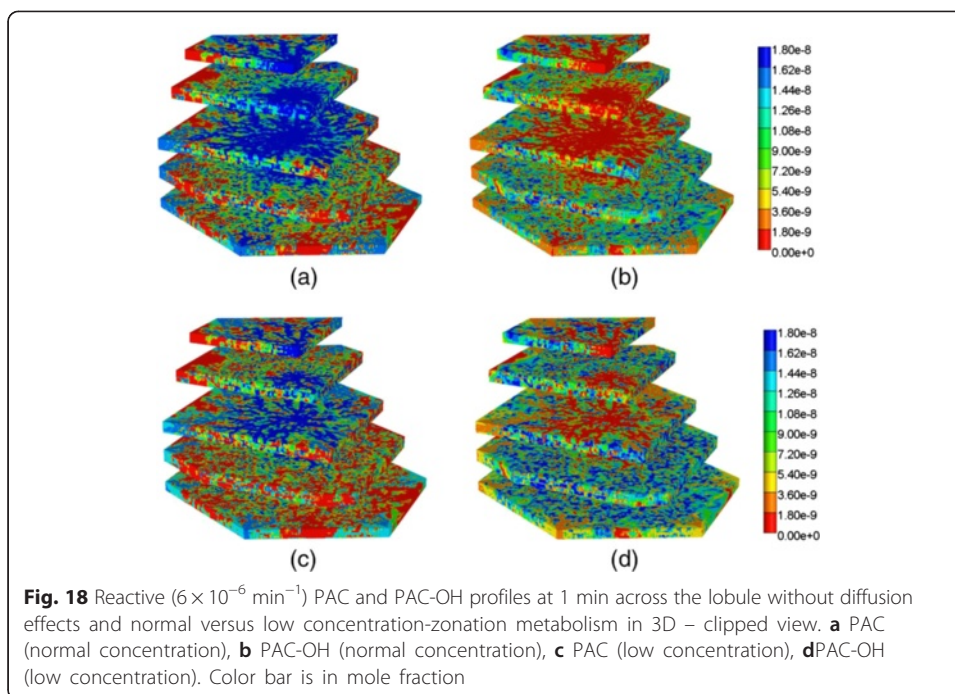
Conclusions

Generalized conclusions relative to our earlier work

The increased morphological variability of the sinusoidal networks generated in this work allows various generalized observations relative to our earlier work on idealized lattice models:

- (a) In 2D due to randomness of the sinusoid patterns, individual producing ports (hepatic veins) respond differently (i.e. at different times) to injected drug. This is similar to the randomness we generated via multiple realizations to our individual well pair models with our previous idealized modelling work. If we sum the individual hepatic vein responses we get an overall 2D lobule drug response (see Fig. 5), the net result of which is an increased spreading (effective diffusion) of the average produced profile.





- (b) Multiple 2D morphological sinusoid realizations can be explored to ascertain the effects of structural variations, as indicated in Table 2. Additionally a 3D model viewed as interacting stacks of 2D sinusoid realizations represents an enhanced method to consider such variability.
- (c) In 3D, because the individual producing ports are completed throughout the vertical extent of the lobule, the variation of response of individual producing ports is seen to be less extreme, although the production curves themselves are more diffuse in 3D than in 2D. Furthermore, the average lobule production summed over all hepatic veins is also more diffuse. Thus the net effect of all these variations is to make the overall response more smooth (i.e. more robust to individual variations).
- (d) When the effect of drug processing (CYP) zonation is included, the effect on drug production characteristics appears quite small and only when the further (smoothing) effects of diffusion are ignored. However, within a lobule we expect there are conditions under which there can be noticeable differences in drug distribution due to zonation. These observations are consistent with our earlier idealized models of zonation. Finally we should emphasize that this treatment of zonation of drug metabolism can be readily extended to other metabolic zonation phenomena occurring in the liver, such as carbohydrate metabolism [21], nitrogen metabolism [22], etc. O_2 distribution is implicated as a fundamental cause of such zonation in all cases.

Follow-up work and future directions

Since various liver diseases can be thought to produce structural variations in the lobule, our analysis also gives insight into the role of disease on liver function and

performance. In our previous work on variable lattice lobule models [9], we utilized random sinusoid permeability models and percolation concepts to capture some of the structural effects of hepatitis and cirrhosis. We next plan on extending such analysis to our more physiologically realistic 3D lobule model.

It should be mentioned that there exist other computer-generated liver models that attempt to provide a realistic representation of the liver vasculature for blood flow and metabolic reaction simulations. Schwan et al. [23] used an image of a mouse liver produced with a CT scanner. Based on this image data, they reconstructed the structure of the fine branches of the liver vessel system. The liver was then split into 50,000 small blocks. The results of the simulation show that blood flow and metabolic reactions can be tracked in detail on the computer monitor. In a follow-up publication [24] a multi-scale model was generated that links together four scales of modeling. Thus the focus of these authors is the full liver scale (organ model) and not the lobule scale (tissue level) which is the subject of our current paper. In addition, we have also recently developed a spatial model of the full liver (White D, Rezania V, Coombe D, Tuszynski J: Building a 3D virtual liver: a preliminary example – methods for describing vascular generation, blood flow calculations, and hepatic clearance, submitted) utilizing a computational algorithm for generating vasculature and where we have considered upscaling from our lobule model and some comparisons with the work of Schwan et al. [23]. Eventually, our overall modeling approach is intended to provide input data regarding liver metabolism for multi-compartment physiologically-based pharmacokinetic models such as those reviewed by Jones et al. [25]. This could lead to more accurate and individualized predictions for the pharmacokinetic analyses of drugs and drug combinations. It is also of interest to explore the possibility of fractal vascular structures and their consequences on the scaling laws in liver function as reviewed extensively by Pang et al. [26].

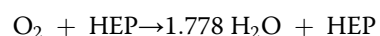
Our focus will continue to be on the structural and metabolic changes induced by liver disease and cancer, and its remediation via drug treatments. More particularly, we will focus on drug combination therapy for cancer (e.g. paclitaxel with doxorubicin) [27].

Appendix A

Reactive O₂ distribution in 3D – indicator of zonation

Here we utilize known O₂ flow characteristics to predict steady state O₂ distributions across our mathematically constructed 3D liver lobule. The O₂ reactive flow characteristics are taken from Davidson et al. [28], and are summarized in Table 3. Davidson et al. [29] utilized this data to analyze O₂ behaviour in their bioartificial liver. Here we will employ the same data to predict O₂ distribution across our 3D lobule model.

The O₂ metabolic reaction used in our model is assumed to be



This approach preserves mass and assumes a non-specific metabolic consumption of O₂ by hepatocytes without detailing explicit cellular metabolic products (since water is a universal component in our model). Reactions occur only in tissue areas (hepatocytes HEP act as “catalysts” for this reaction).

Table 3 O₂ kinetic elimination Michaelis-Menten parameters plus diffusion (converted from Davidson et al. [28], their Table 1)

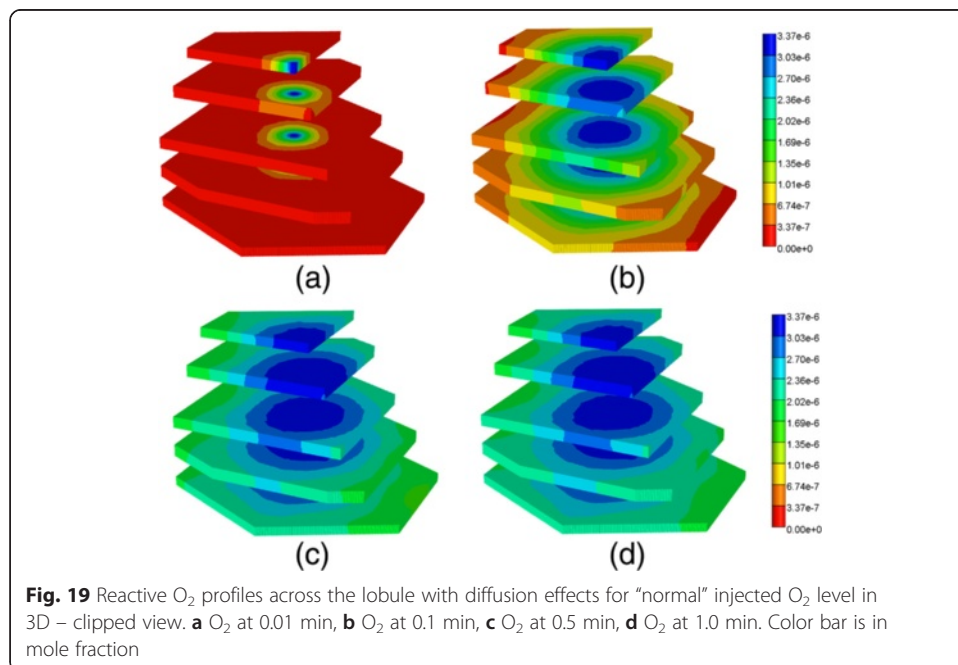
Parameter	Characteristic unit	STARS unit
Maximum Rate v_{max}	352 $\mu\text{M}/\text{min}$	6.34×10^{-6} mole fraction/min
Half Saturation Constant K_m	6.24 μM	1.12×10^{-7} mole fraction
Linear Rate v_{max}/K_m	56.4 min^{-1}	56.4 min^{-1}
Sinusoid Effective Diffusion	3.0×10^{-9} m^2/sec	1.8×10^{-3} cm^2/min
Tissue Effective Diffusion	2.0×10^{-9} m^2/sec	1.2×10^{-3} cm^2/min

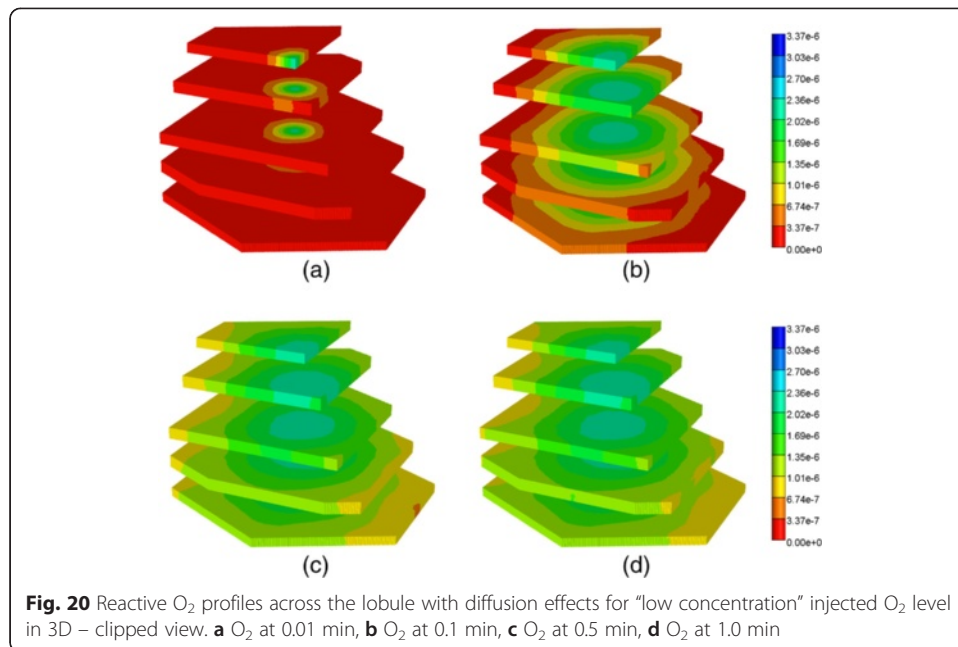
With these parameters, the flow of O₂ across the lobule is calculated in a manner similar to that of reactive PAC. O₂ levels are due to the relative contribution of convection, diffusion and hepatocyte O₂ consumption. Note, however, the flow pattern of O₂ can be expected to be quite different from that of PAC, both because of its reaction rate but also because of its diffusion coefficient, as this is a very small molecule with much higher diffusion than PAC. Here we establish a steady state O₂ distribution throughout the 3D lobule by observing the long time O₂ distribution.

Two cases are considered: (a) “normal” O₂ injection levels, and (b) “low concentration” O₂ injection levels to represent some nonspecific illness condition, as listed in Table 3. [(a) 90 mm Hg = 3.37×10^{-6} mole fraction; (b) 60 mm Hg = 2.25×10^{-6} mole fraction]. Figures 19 and 20 illustrate the evolution of O₂ profiles across the lobule to steady state for these two cases, respectively. Although there are observable concentration differences between the two cases throughout the lobule, the major differences occur near the injection site.

Rescaled versions of these distributions are used to define corresponding predicted CYP distributions. The actual form of this rescaling is

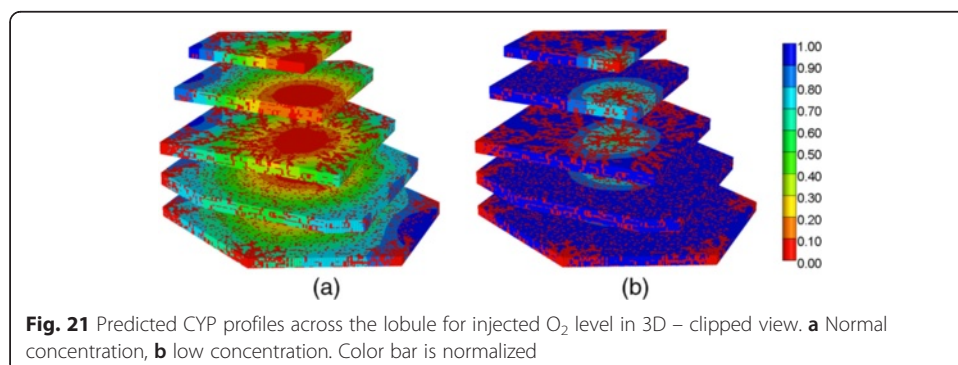
$$[\text{CYP}] = 1.0 \cdot ([\text{O}_2] - [\text{O}_2]_{\min}) / ([\text{O}_2]_{\max} - [\text{O}_2]_{\min})$$





Here $[O_2] > 0$ represents the steady state O₂ concentration level at any location throughout the lobule for each case, while $[O_2]_{\min}$ and $[O_2]_{\max}$ correspond to the non-zero minimum and maximum injected O₂ concentration level for the "normal" case (90 mm Hg = 3.37×10^{-6} molefrac), respectively. Figure 21 shows the resultant CYP profiles for each case. First, there are zero CYP expressed in the sinusoids and near the injection end for the "normal O₂ generated" zonation. There are higher CYP levels generated near the production ports, but the individual CPY levels depend on the flow distribution to each port (the ports with highest flow have lower CYP levels). In contrast, for the "normal O₂ generated" zonation, there is significantly higher levels of CYP predicted and a much more uniform distribution (except closest to the inlet port).

These zonal CYP distributions are used in the main body of the paper to investigate PAC drug zonation effects.



Additional files

Additional file 1: Figure S1. Non-reactive PAC profiles across the lobule with diffusion. (a) PAC at 0.01 min, (b) PAC at 0.1 min, (c) PAC at 0.2 min (d) PAC at 0.5 min. Color bar is in molfrac. (PPTX 206 kb)

Additional file 2: Figure S5. Non-reactive PAC profiles across the lobule without diffusion in 3D – block view. (a) PAC at 0.01 min, (b) PAC at 0.05 min, (c) PAC at 0.1 min (d) PAC at 1 min. Color bar is in molfrac. (PPTX 613 kb)

Additional file 3: Figure S2. Non-reactive PAC profiles across the lobule with diffusion in 3D – block view. (a) PAC at 0.01 min, (b) PAC at 0.05 min, (c) PAC at 0.1 min (d) PAC at 1 min. Color bar is in molfrac. (PPTX 431 kb)

Additional file 4: Figure S3. Non-reactive PAC profiles across the lobule with diffusion in 3D – sliced view. (a) PAC at 0.01 min, (b) PAC at 0.05 min, (c) PAC at 0.1 min (d) PAC at 1 min. Color bar is in molfrac. (PPTX 335 kb)

Additional file 5: Figure S6. Reactive ($6 \times 10^{-3} \text{ min}^{-1}$) PAC and PAC-OH profiles across the lobule without diffusion effects and base case metabolism in 3D – block view. (a) PAC at 0.01 min, (b) PAC at 0.05 min, (c) PAC at 0.1 min, (d) PAC at 1 min, (e) PAC-OH at 0.01 min, (f) PAC-OH at 0.05 min, (g) PAC-OH at 0.10 min, (h) PAC-OH at 1 min. Color bar is in molfrac. (PPTX 1050 kb)

Additional file 6: Figure S4. Reactive ($6 \times 10^{-3} \text{ min}^{-1}$) PAC and PAC-OH profiles across the lobule with diffusion effects and base case metabolism in 3D – sliced view. (a) PAC at 0.1 min, (b) PAC at 0.5 min, (c) PAC at 1 min, (d) PAC-OH at 0.1 min, (e) PAC-OH at 0.5 min, (f) PAC-OH at 1 min. Color bar is in molfrac. (PPTX 378 kb)

Competing interests

The authors declare that they have no competing interests.

Authors' contributions

VR: Primary investigator who conducted the majority of the simulations and model development. DC: Investigator providing technical support for the simulations and model development. JT: Lead investigator who supervised the work content and model development. All authors read and approved the final manuscript.

About the authors

Vahid Rezania: received his PhD in theoretical physics from Institute for Advanced Studies in Basic Sciences, Iran, in 2000. He was research fellow at the University of Alberta, Canada, from 2001 to 2006. He is currently an associate professor in physics at the department of physical sciences of MacEwan University, Canada. His research interests include theoretical physics, biophysics, mathematical and computational modeling.

Dennis Coombe: received his PhD in theoretical physical chemistry from the University of British Columbia in 1976. He was NATO postdoctoral fellow at the Molecular Physics Department of the University of Leiden, the Netherlands from 1976 to 1978. He joined the Computer Modelling Group, Calgary Canada in 1980 and since that time he has been a principle developer of the STARS reservoir simulation software specializing in the modelling of chemical and thermal enhanced oil recovery (EOR) processes. More recently he has expanded his research interests to include microbial EOR modelling, mechanical and blood/metabolite flow in bone and the intervertebral disk, and computational modeling of the liver.

Jack A. Tuszynski: received his M.Sc. with distinction in Physics from the University of Poznan (Poland) in 1980. He received his Ph.D. in Condensed Matter Physics from the University of Calgary in 1983. He did a Post-Doctoral Fellowship at the University of Calgary Chemistry Department in 1983. He was an Assistant Professor at the Department of Physics of the Memorial University of Newfoundland from 1983 to 1988, and at the University of Alberta Physics Department from 1988 to 1990, an Associate Professor from 1990 to 1993 and a Full Professor since 1993. He joined the Division of Experimental Oncology within the Cross Cancer Institute as the Allard Chair in 2005. He is on the editorial board of the Journal of Biological Physics, Journal of Biophysics and Structural Biology (JBSB), Quantum Biosystems, Research Letters in Physics, Water: a Multidisciplinary Research Journal and Interdisciplinary Sciences-Computational Life Sciences. He is an Associate Editor of The Frontiers Collection, Springer-Verlag, Heidelberg.

Acknowledgements

J.A.T. acknowledges funding support for this project from NSERC. The Allard Foundation and the Alberta Advanced Education and Technology.

Author details

¹Department of Physical Sciences, MacEwan University, Edmonton, AB T5J 4S2, Canada. ²Computer Modelling Group Ltd, Calgary, AB T2L 2A6, Canada. ³Department of Physics and Experimental Oncology, University of Alberta, Edmonton, AB T6G 2J1, Canada.

Received: 17 September 2015 Accepted: 22 February 2016

Published online: 03 March 2016

References

1. Ierapetritou MG, Georgopoulos PG, Roth CM, Androulakis IP. Tissue-level modeling of xenobiotic metabolism in liver: an emerging tool for enabling clinical translational research. *Clin Transl Sci.* 2009;2(3):228.
2. Rani HP, Sheu T, Chang TM, Liang PC. Numerical investigation of non-Newtonian microcirculatory blood flow in hepatic lobule. *J Biomechanics.* 2006;39:551.
3. Yan L, Ropella GE, Park S, Roberts MS, Hunt CA. Modelling and simulation of hepatic drug disposition using a physiologically based. *Multi Agent In Silico Liver Pharmaceutical Res.* 2007;25:1023.
4. Wambaugh J, Shah I. Simulating microdosimetry in a virtual hepatic lobule. *J Biomechanics.* 2010;6(4):e1000756.

5. Hoehme S, Brulport M, Bauer A, Bedawy E, Schormann W, Gebhardt R, et al. Prediction and validation of cell alignment along microvessels as order principle to restore tissue architecture in liver regeneration. *PNAS*. 2010;107:10371.
6. Schliess F, Hoehme S, Henkel SG. Integrated metabolic spatial-temporal model for the prediction of ammonia detoxification during liver damage and regeneration. *Hepatology*. 2014;60:2040.
7. Drasdo D, Hoehme S, Hegstler JG. How predictive quantitative modelling of tissue organization can inform liver disease pathogenesis. *J Hepatology*. 2014;61:951.
8. Rezania V, Marsh RE, Coombe D, Tuszynski JA. A physiologically-based flow network model for hepatic drug elimination I: regular lattice lobule model. *Theor Biol Med Model*. 2013;10:52. doi:10.1186/1742-4682-10-52.(PaperI).
9. Rezania V, Marsh RE, Coombe D, Tuszynski JA. A physiologically-based flow network model for hepatic drug elimination II: variable lattice lobule models. *Theor Biol Med Model*. 2013;10:53. doi:10.1186/1742-4682-10-53.(PaperII).
10. Saxena R, Theise ND, Crawford JM. Micro-anatomy of the human liver – exploring the hidden interfaces. *Hepatology*. 1999;30:1339.
11. Bhunchet E, Wake K. The portal lobule in rat liver fibrosis: a re-evaluation of the liver unit. *Hepatology*. 1998;27(2):481–7.
12. Teutsch HF. The modular microarchitecture of human liver. *Hepatology*. 2005;42:317.
13. MATLAB: www.mathworks.com.
14. CMG. Ltd. STARS User's Guide: advanced process and thermal reservoir simulator. Calgary, AB: Computer Modelling Group Ltd; 2014.
15. Gebhardt R. Metabolic zonation of the liver – regulation and implications for liver function. *Pharmacol Ther*. 1992;53(3):275.
16. Jungermann K, Thurman R. Oxygen: modulator of metabolic zonation and disease in the liver. *Hepatology*. 2000;31(2):255.
17. Rowinsky EK, Wright M, Monsarrat B, Lesser GJ, Donehower RC. Taxol: Pharmacology, metabolism, and clinical implications. *Cancer Surv*. 1993;17:283–304.
18. Huizing MT, Misser VH, Pieters RC, ten Bokkel Huinink WW, Veenhopf CH, Vermorken JP, et al. Taxanes: a new class of antitumour agents. *Cancer Invest*. 1995;13:381–404.
19. Vaclavikova R, Soucek P, Svobodova L, Anzenbacher P, Simek P, Guengerich F, et al. Different in vitro metabolism of paclitaxel and docetaxel in humans, rats, pigs, and minipigs. *Drug Metab Dispos*. 2004;32(6):666–74.
20. Monsarrat B, Chatelut E, Royer I, Alvinerie P, Dubois J, Dezeus A, et al. Modification of paclitaxol metabolism in cancer patient by induction of cytochrome P450 3A4. *Drug Met Disp*. 1998;26:229–33.
21. Jungermann K, Thurman R. Hepatocyte heterogeneity in the metabolism of carbohydrates. *Enzyme*. 1992;46:33.
22. Haussinger D, Lamers W, Moorman A. Hepatocyte heterogeneity in the metabolism of amino acids and ammonia. *Enzyme*. 1992;46:72.
23. Schwen LO, Krauss M, Niederalt C, Gremse F, Kiessling F, et al. Spatio-temporal simulation of first pass drug perfusion in the liver. *PLoS Comput Biol*. 2014;10(3):e1003499. doi:10.1371/journal.pcbi.1003499.
24. Schwen LO, Schenk A, Kreutz C, Timmer J, Bartolomé-Rodríguez MM, Kuepfer L, et al. Representative sinusoids for hepatic four-scale pharmacokinetics simulations. *PLoS ONE*. 2015;10(7):e0133653. 1–39.
25. Jones HM et al. A novel strategy for physiologically based predictions of human pharmacokinetics. *Clin Pharmacokinet*. 2006;45(5):511–42.
26. Pang KS, Weiss M, Macheras P. Advanced pharmacokinetic models based on organ clearance, circulatory, and fractal concepts. *AAPS J*. 2007;9(2):E268–83.
27. Vos KJ, Martin AG, Trimbol MG, Forestell L, Barakat K, Tuszynski JA. A multi-compartment pharmacokinetic model of the interaction between paclitaxel and doxorubicin. *EPJ Nonlinear Biomed Phys*. 2014;2:13.
28. Davidson AJ, Ellis MJ, Chaudhuri JB. A theoretical method to improve and optimize the design of bioartificial livers. *Biotech Bioeng*. 2010;106(6):980.
29. Davidson AJ, Ellis MJ, Chaudhuri JB. A theoretical approach to zonation in a bioartificial liver. *Biotech Bioeng*. 2011;109(1):234.

Submit your next manuscript to BioMed Central and we will help you at every step:

- We accept pre-submission inquiries
- Our selector tool helps you to find the most relevant journal
- We provide round the clock customer support
- Convenient online submission
- Thorough peer review
- Inclusion in PubMed and all major indexing services
- Maximum visibility for your research

Submit your manuscript at
www.biomedcentral.com/submit

